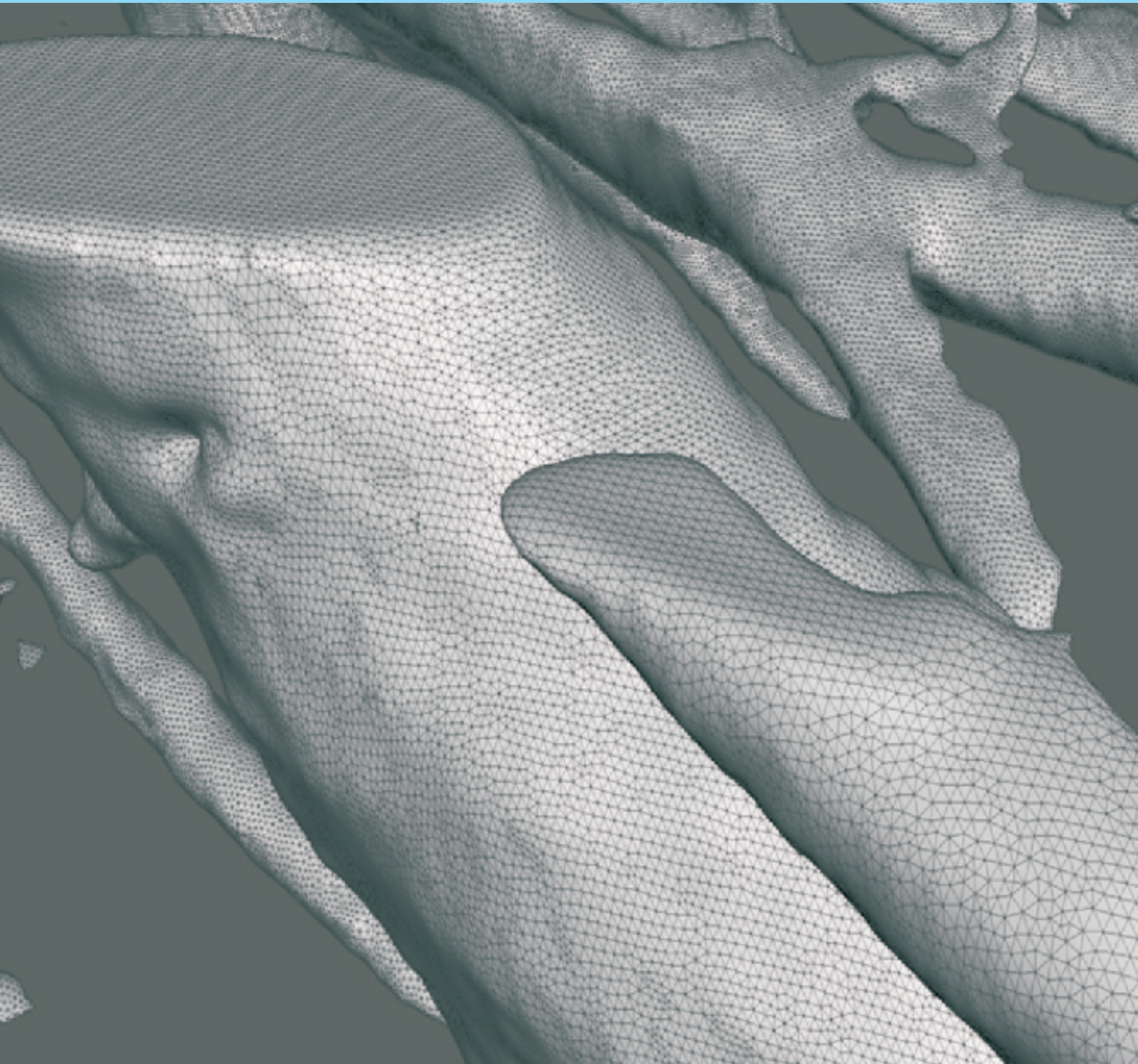


BARC newsletter

Volume 374 | Mar-Apr 2021 | ISSN:0976-2108

- Compatibility of materials in molten salts for MSBR applications
- Model Transfer Cask for Automated Handling of Canisters in Storage Vaults
- In-situ X-ray micro tomography facility at imaging beamline Indus-2



Science News
Climate change impact on glacier melting in Himalayas



Technology Transfer
Spot Picker Robot for Proteomics Applications



This page is intentionally left blank

BARC newsletter

Volume 374 | Mar-Apr 2021 | ISSN:0976-2108

RESEARCH ARTICLES

1. **Facility to test the compatibility of materials in molten salts for MSBR applications**

Dr.(Smt.) Poulami Chakraborty *et al*

10. **Development and Demonstration of Model Transfer Cask for Automated Handling of Canisters in Storage Vaults**

Shri. Kiran T. Badgujar *et al*

16. **Development of In-situ X-ray imaging and μ -CT facility under load conditions at imaging beamline Indus-2**

Dr. Ashish K. Agarwal *et al*

TECHNOLOGY TRANSFER

21. **Spot Picker Robot for Proteomics Applications**

Dr. R.S. Sengar

SCIENCE NEWS

22. **Climate change impact on glacier melting in Himalayas**

Dr. Tirumalesh Keesari



Bird's eye view of
Bhabha Atomic Research Centre
Mumbai



The In-situ X-ray μ -CT facility
at imaging beamline
BL-4, Indus-2



The sliding door equipped with two drives,
a part of Automated Transfer Cask System

On the Cover
*3D volume mesh data
of compressed Aluminium
sample*

@ BARC Photo

This page is intentionally left blank

Editorial Committee

Chairman

Dr. A.P. Tiwari
KMG

Editor

Dr. G. Ravi Kumar
SIRD

Members

Dr. A.K. Nayak, RED
Dr. G. Sugilal, PSDD
Dr. V.H. Patankar, ED
Dr. (Smt.) B.K. Sapra, RP&AD
Dr. L.M. Pant, NPD
Dr. Ranjan Mittal, SSPD
Dr. (Smt.) S. Mukhopadhyay, ChED
Dr. K.P. Muthe, TPD
Dr. V. Sudarsan, ChD
Dr. A.V.S.S.N. Rao, AGS
Dr. S.R. Shimjith, RCnD
Dr. Sandip Basu, RMC
Dr. Pranesh Sengupta, MSD
Dr. R. Tripathi, RCD

Member Secretary & Coordination

Madhav N, SIRD

Art, Design, Creative Work

Dinesh J. Vaidya, SIRD
Madhav N, SIRD

editor's MESSAGE



This issue of BARC Newsletter comprises five articles based on a wide variety of research and development activities carried out in BARC. The front cover of this issue features the three dimensional volume mesh data of compressed Aluminium sample based on studies carried out at the in-situ X-ray micro tomography facility at Indus-2. We express our sincere gratitude to all those who have contributed to the articles for this issue and to the reviewers who have spent time to make this issue possible.

Facility to test the compatibility of materials in molten salts for MSBR applications

Poulami Chakraborty¹, Rumu H. Banerjee¹, Nachiket Keskar², Raghvendra Tewari¹ and Vivekanand Kain³

¹Materials Science Division, ²Mechanical Metallurgy Division, ³Materials Group
Bhabha Atomic Research Centre, Mumbai-400085

Corresponding author & Email : Poulami Chakraborty, poulamic@barc.gov.in

ABSTRACT

Understanding the corrosion behavior of structural materials in molten fluoride salts like FLiNaK is crucial for the development of the Molten Salt Breeder Reactor (MSBR). However, handling of molten fluoride salts during long term experimentation is quite challenging due to their high reactivity with oxygen and moisture which is even greater than that of liquid metals and alloys. In this regard, a unique glove box coupled molten salt corrosion test facility (MSCTF) with automatic sample exchange system has been designed, developed and installed at Materials Group, BARC. All wetted parts of this facility were made up of pure nickel, and provision had been made to conduct molten salt corrosion experiments under controlled atmosphere at temperatures up to 1273 K (1000°C). Various Ni based alloys including the indigenously developed Ni-Cr-Ti-Mo alloy have been exposed to molten FLiNaK salt under static condition in MSCTF and few salient results are presented in this paper.

Keywords: Molten Salt, Corrosion, FLiNaK, Hastelloy, Ni-Cr-Mo-Ti

Introduction

In order to meet the demand for a sustainable source of carbon-free energy, various advanced nuclear reactors are being designed across the globe [1]. One of the most promising candidates in this fleet is Molten Salt Reactor (MSR) [2-3]. The major advantage of MSR comes from its liquid fuel characteristics such as (i) negative temperature coefficient of reactivity, (ii) facilitates online fuel reprocessing, and (iii) allows efficient utilization of fertile thorium [1-4]. MSR is associated with an inherent safety feature since it can passively regulate its own temperature [4]. In a scenario where the reactor gets overheated, the reactivity of the core automatically comes down thus making the temperature coefficient of reactivity negative [2-3, 5]. Keeping this in mind and with an aim to efficiently utilize its abundant thorium reserves, India has initiated MSR development program and proposed a conceptual design of Indian Molten Salt Breeder Reactor (IMSBR) [5-6].

The fuel salt for IMSBR is generally a mixture of fluorides of Uranium, Thorium and Lithium while the eutectic mixture of LiF, KF and NaF (46.5% LiF–11.5% NaF–42% KF also known as FLiNaK) has been selected as the

coolant salt for this system [3,5-6]. The major advantage of using molten fluoride salt is its better thermo-physical properties viz., high thermal conductivities, high specific heats, low viscosities, low vapour pressure (<1 atm), high boiling points and favourable neutronic properties viz. neutron absorption cross-section, irradiation stability etc [7]. However, corrosion of structural materials in molten fluoride salt environment is considered as a major issue in practical realisation of such MSBR system [8]. This is because of the fact that the reaction products formed by the fluorination of the alloying metals are soluble in the salt. Thus, the protective oxide film available at the material surface becomes chemically unstable in the presence of fluoride salt leading to thermodynamically driven dissolution of alloying elements in the molten salt and vice-versa [8-9].

In general, nickel based alloys, due to their satisfactory compatibility towards liquid fluoride salt combined with excellent high temperature mechanical properties, are proposed as structural materials for molten salt systems [9-10]. Researchers across the globe are working on fine tuning the composition of readily available Ni based alloys, like Hastelloy N and Inconel 800, to optimise the structural and mechanical properties which are best suited

for the operating temperature regime of molten salt reactors (923 K to 1273 K i.e. 650°C to 1000°C) [11-12]. In this context, a novel Ni based alloy with Mo, Cr and Ti as the principle alloying elements has been developed as the candidate (structural material) of the IMSBR [13,14]. The alloy (Ni-11Mo-7Cr-2.4Ti) was prepared using vacuum induction melting (VIM) route and its microstructural as well as welding characteristics have been investigated in detail [13-14]. Understanding the corrosion behavior of this alloy in molten fluoride salts like FLiNaK within the regime of reactor operating parameters is extremely crucial for the development of IMSBR. The biggest challenge, related to the handling of molten fluoride salts during experimentation and storage involves their high reactivity with oxygen and moisture which is even greater than that of liquid metals and alloys [7]. Keeping this in mind, a unique glove box coupled molten salt corrosion test facility has been designed, developed and installed at Materials Group, BARC. The facility provides an opportunity for long term corrosion testing of structural

and functional materials in molten salts (fluorides, chlorides, nitrates) under static conditions at elevated temperatures up to 1273 K (1000°C). The present report provides a detailed overview of the construction and working of this facility and presents the initial results from molten salt corrosion experiments carried on various imported Ni based alloys as well as the indigenously prepared Ni-Cr-Mo-Ti alloy.

Description of Experimental facility

Figure 1 shows the schematic of a fully automated Molten Salt Corrosion Test Facility (MSCTF) which facilitates static compatibility testing under inert gas atmosphere as well as in vacuum ($\sim 10^{-6}$ mbar). It also incorporates the feature of automatic sample immersion/exchange thereby overcoming the challenge of sample insertion/removal at high temperature keeping the controlled atmosphere intact.

As shown in Figure 1, a double chamber retort (144 mm outer diameter (OD) x 450 mm long x 12 mm thick) made

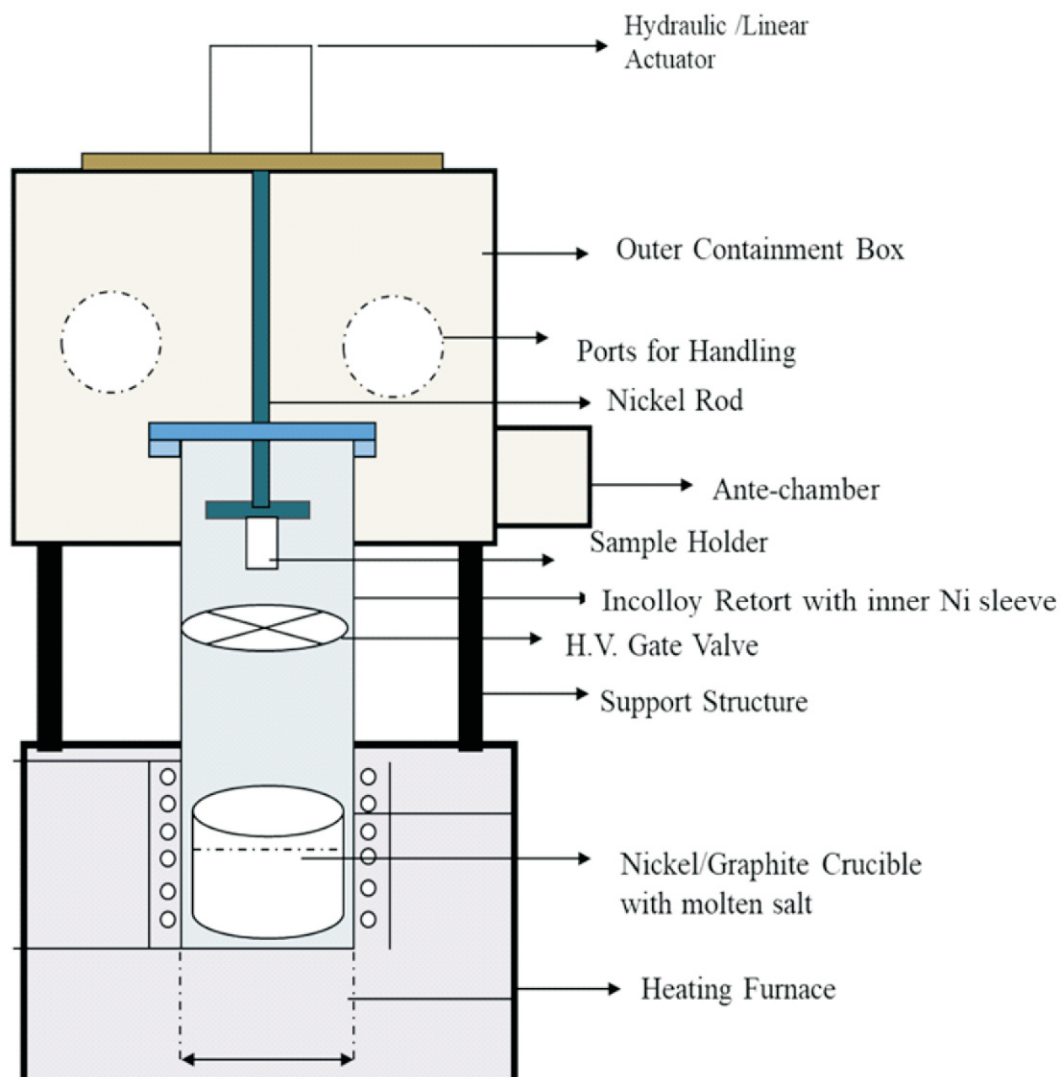


Fig. 1: Schematic of molten salt corrosion test facility (MSCTF)

out of Incolloy 800 is located at the heart of the MSCTF. Incolloy 800 has been chosen as the material of construction for this retort as it can withstand high temperatures during continuous operation for prolonged duration (~ 5000 h). The retort is completely covered from inside with a 6 mm thick pure Nickel sleeve which is known to be resistant to fluoride attack and to minimise galvanic corrosion due to dissimilar metal contact with the molten salt [15]. For example, a study by Olson et al. showed that the corrosion rate in Hastelloy N with graphite crucible at 850°C is $45.5 \pm 4.0 \mu\text{m}/\text{year}$ while with Ni crucible, the rate is $15.8 \mu\text{m}/\text{year}$ [16]. A crucible (100 mm OD x 100mm long x 3mm thick) containing the molten salt is kept at the bottom of this retort where its temperature could be raised up to 1000°C by a heating furnace. At present, the crucibles for holding molten fluoride salts are made of pure nickel, although there is a provision to customise the material of construction as per the operating conditions. The nickel crucible is held in a crucible cage which increases the ease of lifting it out of the retort during replacement of salt. Dedicated holders made out of pure nickel are used for holding the corrosion coupons. As shown in Figure 3, various geometries of holders are available for holding single or multiple samples at a time.

The sample holder is fixed to a pure nickel rod which is connected to a linear actuator system responsible for the insertion and removal of samples inside molten salt. In order to prevent moisture ingress into the salt during preparation and handling, the entire top portion of the retort is enclosed in a tailor-made glove box which facilitates sample exchange and salt preparation under controlled atmosphere. The inert gas is passed through silica gel based moisture purifier and catalyst based

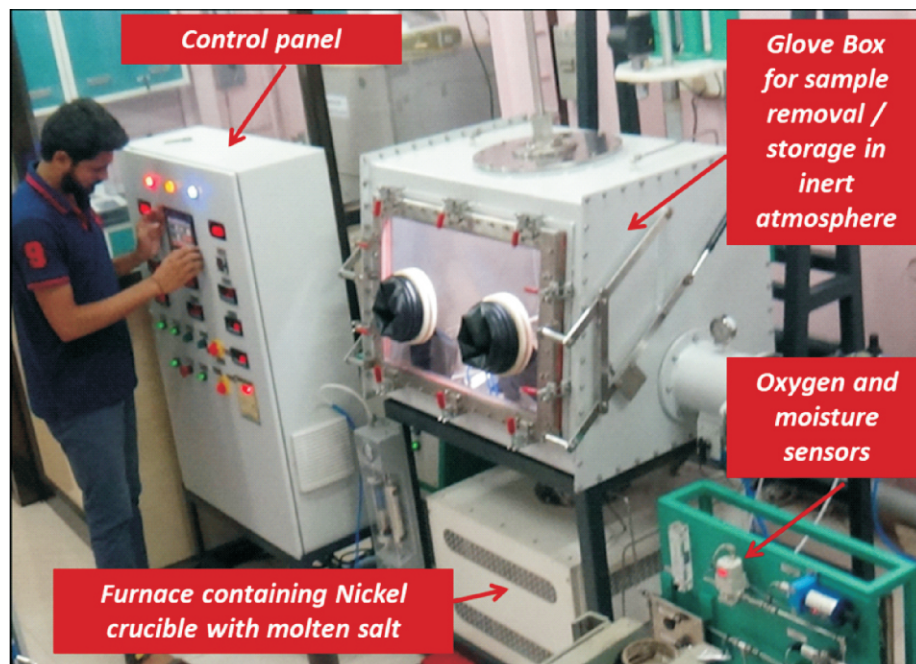


Fig. 2: The molten salt corrosion test facility developed in Materials Science Division, BARC

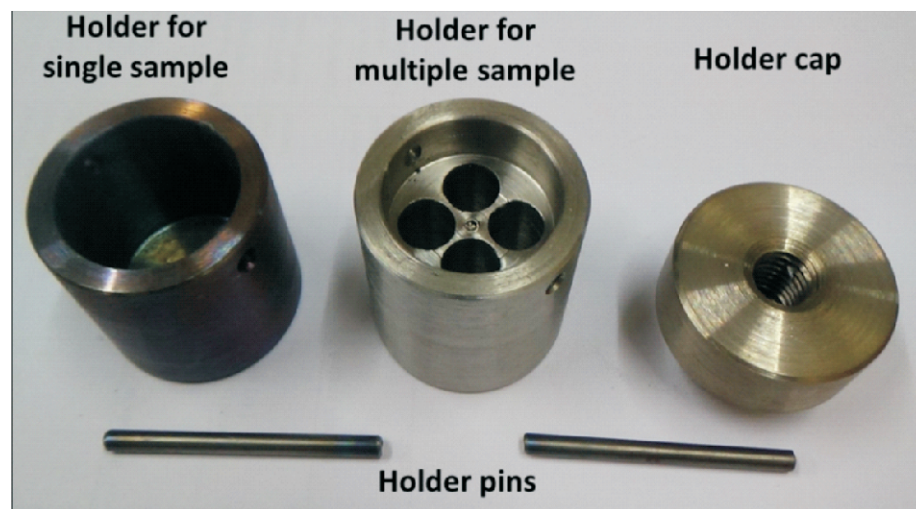


Fig. 3 : Different sample holders of molten salt compatibility testing (MOC: Nickel)

oxygen purifiers before introducing into the retort or glove box. Dedicated moisture and oxygen sensors are placed in the inlet and outlet gas lines of the retort to monitor the experimental conditions. Intermittent purging by dry argon gas helps to maintain an inert environment during molten salt corrosion experiment as well as to carry possible gaseous HF away from the autoclave as outlined by Ouyang *et al.* [17].

A special feature of the MSCTF system is a pneumatically operated high vacuum gate valve (MOC: Incolloy 800H)

which can separate the Incolloy retort into two halves when the samples are held in the upper chamber. During the start of an experiment, the valve is kept closed and the samples holder with samples fixed to the nickel rod is kept in the upper half of the retort (i.e. above the HV gate valve). Thereafter, the salt in the nickel crucible is allowed to melt under inert atmosphere. During melting, the salt is heated in a stepwise manner to the operating temperature to ensure only minimal oxide impurities get generated by the accelerated reaction of residual moisture with the salt during the heating process. The temperature of the salt is measured by a K-type thermocouple connected to the inner surface of the Incolloy Retort. After melting, both parts of the retorts are brought under similar controlled atmospheric conditions before opening of the valve and lowering the sample holder to the bottom half to dip it inside molten salt for the required duration of exposure. Conductance based level indicators have been installed at various locations to monitor and control the movement of the sample holding rod. Once the experiment is completed, samples are brought to the upper part and the valve is closed back. Under the closed condition of the valve, top cover flange of the retort could be opened and the samples can be removed or fresh samples could be loaded. This arrangement allows to keep the salt in molten state without exposing it to outside atmosphere during sample exchange. The presence of glove box containment provides an additional layer of safety allowing removal of the samples and handling of the salt under inert atmosphere for sampling/refilling as and when required.

Special kind of seals are designed for this system which allow movement of the sample holders through the top

flange covering the retort as well as the glove box without breaking the controlled atmosphere. The major flanges of the retort including the valve flange as well the retort cover flange are cooled by a recirculating chilled water to maintain the ambient temperature. The entire operation of the system is automatically controlled through PLC based controllers which operates through a compact LCD type touch screen interface. All required interlocks and indicators have been incorporated to ensure operational safety. The above discussed arrangement helps to make the sample exchange process fast, simple and efficient in addition to repeated usage of the set-up for conducting multiple experiments.

Experiments Conducted

The MSCTF system has been successfully commissioned and several experiments have been conducted in FLiNaK salt. In the initial stage of commissioning, FLiNaK salt has been prepared in 500 g scale as shown in Figure 2. In order to reduce the contamination of moisture to a minimum, the powders of individual salts (LiF, KF and NaF) have been introduced inside the glove box of MSCTF and dehydrated in high purity argon atmosphere. The salt was later prepared by mixing the powders in eutectic composition (46.5 mol% LiF–11.5 mol.% NaF–42 mol% KF) and heating the mixture at 873 K (600 °C). The melting point of the resultant salt mixture was found to be 729 K (456 °C) which was very close to the melting pint of FLiNaK (727 K or 454 °C). The impurity content of the prepared salt was analysed through ICP-MS and is listed in Table 1. Fig. 4 gives a photograph of the FLiNaK salt held in the nickel crucible inside MSCTF.



Fig. 4: FLiNaK salt prepared in MSCT Facility

Composition of FLiNaK salt prepared in MSCTF obtained through ICP-MS (Table 1)

Al (%)	Cr (ppm)	Cu (ppm)	Fe (ppm)	Mn (ppm)	Ni (ppm)	Li (%)	Na (%)	K (%)	F (%)
0.33	14.1	11.1	332.5	6.4	<7	9.49	12.76	13.82	38.6

List of materials exposed to FLiNaK in MSCTF till date (Table 2)

S.No	Materials	Temperature (K)	Duration (h)	Atmosphere
1.	Hastelloy N	973	72	High Purity Argon
2.	Hastelloy X	973	72	High Purity Argon
3.	Ni-Cr-Mo-Ti alloy	973	50	High Purity Argon
4.	Ni-Cr-Mo-Ti alloy (welded)	973	50	High Purity Argon

Composition of various materials exposed in FLiNaK inside MSTCF (Table 3)

	Ni	Mo	Cr	Ti	Fe	Si	Mn	V	C	Cu	W	Al	Nb
Hastelloy N (Imp)	bal	16.11	6.31	<0.01	4.03	0.38	0.53	0.02	0.03	0.01	0.06	<0.01	NA
Hastelloy X	bal	8.76	21.34	0.01	19.29	0.58	0.54	-	0.59	-	0.4	0.08	NA
Ni-Cr-Mo-Ti alloy	bal	11.07	7.16	2.42	0.073	0.13	0.23	NA	0.03	NA	NA	0.25	0.25

Various samples of commercially available Hastelloy along with the indigenously produced Ni-Cr-Mo-Ti alloy have been exposed to FLiNaK in this facility. The effect of welding on the molten salt compatibility of Ni-Cr-Mo-Ti alloy has also been studied by exposing samples having a bead on plate by Tungsten Inert Gas (TIG) welding on them. The TIG welding was carried out at a voltage of 15 V with a current of 70 A using a filler of the same composition as the base material. The temperature of exposure has been chosen to be 973 K (700°C) for the present experiments since this falls within the operating regime of IMSBR and a large corrosion database of Ni based alloys in fluoride salts is available at this temperature [5,9-10, 18]. Table 2 gives the list of experiments carried out in this facility till date along with the experimental parameters while Table 3 gives the composition of each material listed in Table 2.

The exposed samples were cleaned off to remove the adherent molten salt by repeatedly exposing them to a 1 M solution of aluminium nitrate (Al(NO₃)₃) and washing with deionized water. Afterwards, the weight loss due to molten salt exposure was measured in order to find the corrosion rate as per equation 1.

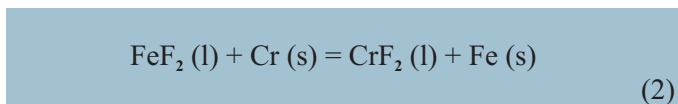
$$\text{Corrosion rate} \left(\frac{\mu\text{g}}{\text{cm}^2 \cdot \text{h}} \right) = \frac{\text{Weight Loss (g)} \times 10^{-6}}{\text{Surface Area exposed (cm}^2\text{)} \times \text{Duration of exposure (h)}} \quad (1)$$

Afterwards, the surface of the samples before and after exposure to molten salt was analysed with the help of Scanning Electron Microscope (SEM) and Electron Back Scattered Diffraction (EBSD).

Results and Discussions

Table 4 enlists the weight loss and corrosion rate of various materials after exposure to FLiNaK in MSCTF at 973 K while figure 5 depicts the variation in corrosion rate in the

form of bar graphs for better comparison. It could be clearly observed from Figure 5 that the molten salt corrosion rate of indigenously produced Ni-Cr-Mo-Ti alloy was comparable to that of imported Hastelloy N and much lesser than that of Hastelloy X, which has the highest chromium content among all the exposed alloys. It should be noted that the corrosion rate in fluoride salt is generally higher in the initial periods of exposure due to presence of impurities as well as due to the presence of a higher fraction of fresh active surface of exposure [8, 9, 18]. The metallic impurities such as Fe, if present in fluoride salt, can selectively leach out Cr via the reaction shown in Equation 2.



Where “l” and “s” stands for liquid and solid phases respectively.

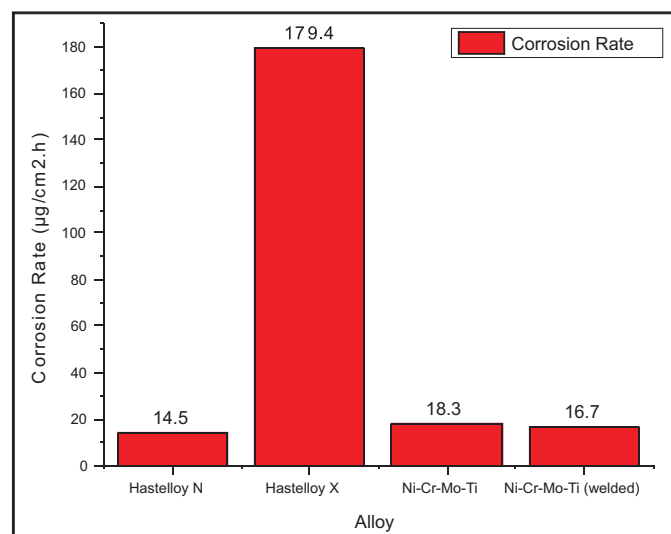


Fig. 5: Corrosion rate of various materials exposed in FLiNaK at 973 K in MSCTF

	Duration (h)	Initial wt. (g)	Final wt. (g)	Wt. loss (g)	Area (cm ²)	Corrosion rate (μg/cm ² .h)
Hastelloy N	72	6.3584	6.3533	0.0051	4.8828	14.50
Hastelloy X	72	7.6577	7.5838	0.0739	5.7132	179.65
Ni-Cr-Mo-Ti	50	3.6701	3.6666	0.0035	3.8521	18.17
Ni-Cr-Mo-Ti (welded)	50	1.4562	1.4543	0.0019	2.2269	17.06

Weight Loss, Exposed Surface Area & Corrosion Rate of materials exposed in FLiNaK at 973 K in MSCTF (Table 4)

However, once the impurities are exhausted, a thermodynamic equilibrium is reached and the corrosion rate decreases (generally for exposure at extended periods of time). Therefore, the corrosion rate of Ni-Cr-Mo-Ti alloy after prolonged duration of exposure (> 500 h) in FLiNaK is expected to be significantly lower than what has been obtained for 50 h exposure in the present case.

Nevertheless, the present experiment has revealed that the presence of TIG welding on Ni-Cr-Mo-Ti alloy did not adversely affect its corrosion resistance. The corrosion rate was found to be rather lower in the case of welded samples as shown in Figure 5. As molten salts are ionic in nature and good electrical conductors, oxidation-reduction reactions will readily occur when these salts act as a medium [9,18-20]. In the presence of an inherent oxidant (ox), fluoride salts generally oxidize the alloying elements (M) in the structural materials like Cr, Ni, Mo, etc, thereby forming their respective fluorides [18-20]. In general, such formation of metal fluorides and their subsequent dissolution in FLiNaK is an irreversible electrochemical process which occurs via Equations 3,4 and 5 [19-20].

Anodic dissolution of metal:



Cathodic evolution of the oxidant in the salt:



Formation of metal fluorides:

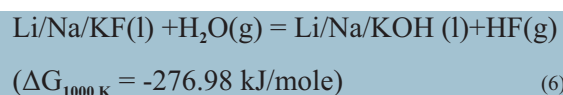


where “Ox” and “Red” represent the oxidant present in the salt (oxidizing impurities like moisture or HF which are inherently present in fluoride salts) and its corresponding reductant respectively while F⁻ in equation 5 is generated from HF or from the salt itself.

The fluoride of the alloying element (M) having higher stability (i.e. lowest free energy, ΔG° in Equation 5) will have a greater tendency for the formation of fluorides in the presence of fluoride salts like FLiNaK [18-20]. Such elements will therefore, be preferentially leached out in the molten salt. The fluoride forming tendencies of the major alloying elements in Ni-based alloys like Hastelloy N are as follows [18]:-

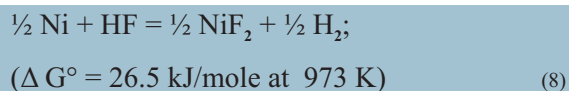
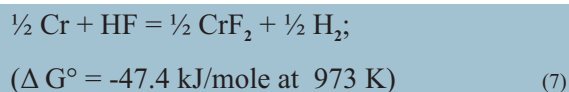


Therefore, it is evident that chromium will have the highest probability of leaching out from structural materials and thus the corrosion rates in FLiNaK as observed in Figure 5 could be directly related to the chromium content of the respective materials. Nevertheless, the corrosive nature of halide salts like fluorides and chlorides are aggravated in the presence of oxidising contaminants like H₂O and HF [18-20]. In fact, the inherent presence of a small quantity of such contaminants in fluoride salts is generally the cause of the initiation of corrosion attack over structural materials as shown in equation 4 [19-20]. Due to the inherent hygroscopic nature of the fluoride salts, they tend to absorb moisture during the production and subsequent storage. As per Equation 6, the presence of moisture in fluoride salts leads to the formation of a highly deleterious corrosive agent, HF [20-21].



Where “l” and “g” stands for liquid and gaseous phases respectively.

The gaseous HF generated is dissolved and strongly retained in the molten fluoride salt which lead to further corrosive attack on the alloying elements of structural materials. Two such reactions with Cr and Ni are shown in equation 7 and 8 [18, 20-21]



Thus, maintaining purity of the salts in terms of oxygen and moisture through a suitable control system is of utmost importance during a molten salt corrosion experiment.

The attack by molten fluoride salt has been found to mainly confine to the grain boundaries during the first 50 h of exposure in the present study. This phenomenon, in fact,

etches the samples so well that all grain boundaries in the weld and base metal could be clearly revealed by the attack [22]. Figure 6 shows SEM micrograph of the exposed surface of welded sample of Ni-Cr-Mo-Ti alloy after exposure to molten FLiNaK at 973 K for 50 h. Even in un-etched condition, the elongated columnar grains of the welded region could be clearly distinguished from the large equiaxed grains of the base material which could be attributed to the preferential attack at the grain boundaries. In addition, pits due to molten salt corrosion were observed in the base metal only [18]. This complemented our result of lower corrosion rate of the welded samples (Figure 5) although such a reduction in the presence of welding is counterintuitive. In order to understand this fact, a detailed grain boundary analysis of the weld and base metal regions of the as-received Ni-Cr-Mo-Ti alloy was conducted through EBSD. Figure 7 shows the fraction of grain boundaries with various mis-orientation angles in weld and base metal regions of Ni-Cr-Mo-Ti alloy. It was clearly

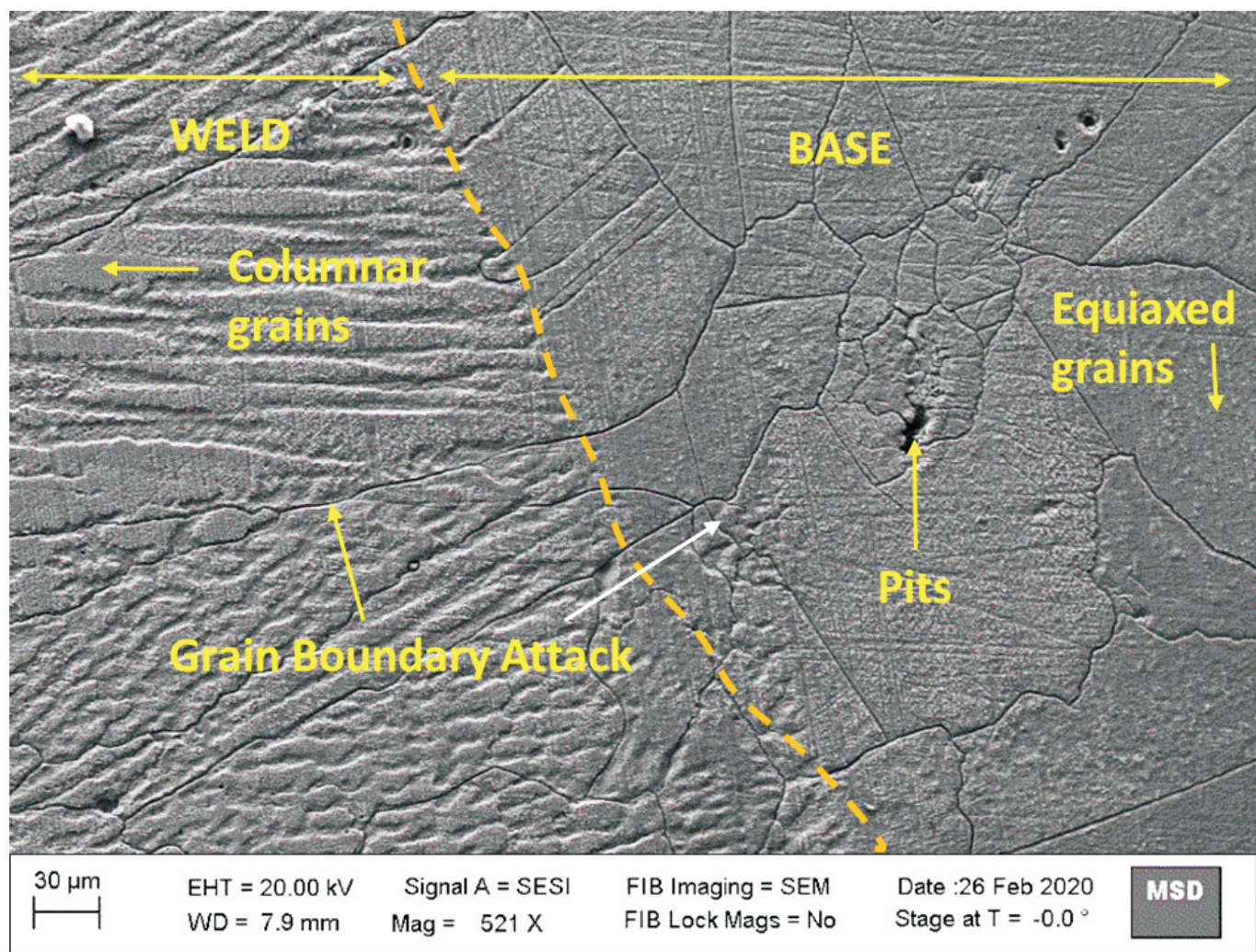


Fig. 6: SEM image of exposed surface of indigenously developed Ni-Cr-Mo-Ti alloy showing grain boundary attack in the weld and base metal

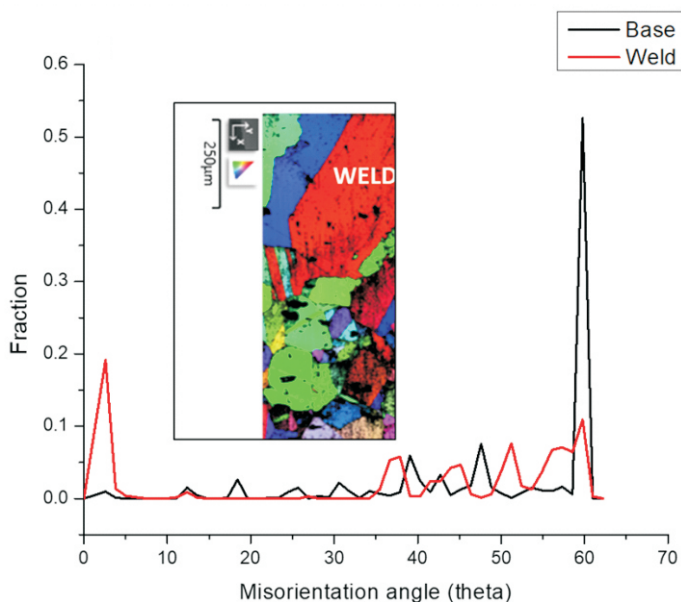


Fig. 7: Fraction of high and low angle grain boundaries in the base metal and weld zone of as-received Ni-Cr-Mo-Ti alloy. Inset shows EBSD map of Ni-Cr-Mo-Ti alloy used for analysis

observed that the fraction of high angle grain boundaries (i.e. with higher mis-orientation angle and higher grain boundary energy) was distinctly lower in the case of the weld region. Since the probability of grain boundary attack is directly related to the energy of the grain boundaries, it is highly possible that reduction in the number of high angle grain boundaries is responsible for decrease in corrosion rate at the welded region [23]. The results from the present study indicate that the alloy microstructure and the grain boundary distribution play a prominent role in the corrosive attack by molten fluoride salt.

Summary

A fully automated Molten salt corrosion test facility (MSCTF) has been developed at Materials Group, BARC. The set up facilitates corrosion testing in molten fluoride and other salts up to 1273 K under inert atmosphere or vacuum. The facility has been successfully commissioned and several corrosion tests in FLiNaK salt have been carried out. The molten salt corrosion behavior of indigenously developed Ni-Cr-Ti-Mo alloy has been tested at 973 K in FLiNaK and found satisfactory. The effect of welding of the molten salt corrosion behavior have also been explored where results showed no reduction in corrosion resistance in the case of welded samples.

References

[1] M. Ho, E. Obbard, P. A. Burrb and G. Yeoh, "A review on the development of nuclear power reactors", *Ennergy Procedia* 160 [2019] 459-466.

[2] K. Furukawa, "Proposal to the development of molten-salt breeder reactor," *Genshiryoku Kogyo* 24 (1) [1978] 9–26.

[3] M. W. Rosenthal, P. R. Kasten, and R. B. Briggs, "Molten-salt reactors—history, status, and potential," *Nucl. Appl. Technology* 8 (2) [1970] 107–117.

[4] B. M. Elsheikh, "Safety assessment of molten salt reactors in comparison with light water reactors," *Journal of Radiation Research and Applied Sciences* 6 (2) [2013] 63–70.

[5] A. Rykhlevskii, J. W. Bae, and K. D. Huff, "Modeling and simulation of online reprocessing in the thorium-fueled molten salt breeder reactor," *Annals of Nuclear Energy*, vol. 128, pp. 366–379, 2019.

[6] P. K. Vijayan, A. Basak, I. V. Dulera, K. K. Vaze, S. Basu and R. K. Sinha, "Conceptual design of Indian molten salt breeder reactor", *PRAMANA - Journal of physics* 85 (3) [2015] 539–554.

[7] A. K. Srivastava, R. Chouhan, A. Borgohain, S. S. Jana, N. K. Maheshwari, D. S. Pilkhwal, A. Rama Rao, K. N. Hareendhran, S. Chowdhury, K. B. Modi, S. K. Raut, S. C. Parida, "An Experimental and Numerical Study to Support Development of Molten Salt Breeder Reactor", *Journal of Nuclear and Radiation Science* 3(3) [2017] 031007 (8).

[8] S. Delpecha, C. Cabet, C. Slim G. S. Picard, "Molten fluorides for nuclear applications", *Materials Today* 13 (12) [2010] 34-41.

[9] V. Ignatiev, A. Surenkov, "Structural Materials for Generation IV Nuclear Reactors. Chapter 5: Corrosion phenomena induced by molten salts in Generation IV nuclear reactors", doi:<http://dx.doi.org/10.1016/B978-0-08-100906-2.00005-7>.

[10] G. Zheng and K. Sridharan, "Corrosion of Structural Alloys in High-Temperature Molten Fluoride Salts for Applications in Molten Salt Reactors", *The Journal of the Minerals, Metals & Materials Society (TMS)*, 70 (8) [2018] 1535-1541.

[11] R. N. Wright., L. Sham, "Status of Metallic Structural Materials for Molten Salt Reactors", <http://www.inl.gov>, INL/EXT-18-45171.

[12] H. E. McCoy, J. R. Weir, "Development of a Titanium-Modified Hastelloy N with Improved Resistance to Radiation Damage," in *Irradiation Effects in Structural Alloys for Thermal and Fast Reactors* (West

- Conshohocken, PA: ASTM International, [1969], 290-311.
- [13] N. Naveen Kumar, V. Singh, H. Donthula, P. Chakraborty, S. Neogy, A. Laik and R. Tewari, N. Keskar, A. Behera, K. V. M. Krishna, R. Kapoor, B. P. Badgujar, A. Basak, M. Krishnan “Development of Ni-Mo-Cr-Ti-C alloy for Indian molten salt breeder reactor”, BARC Internal Report, BARC/2020/I/028 [2020].
- [14] N. Keskar, K. V. Mani Krishna, B.P. Badgujar, M. N. Jha, S. Kumar, A. Laik, R. Tewari, J. B. Singh and M. Krishnan, “Laser and Electron beam (EB) welding studies on NiCrMoTi alloy”, BARC Internal Report, BARC/2020/I/029 [2020]
- [15] L. Olson, K. Sridharan, M. Anderson, T. Allen, “Nickel-plating for active metal dissolution resistance in molten fluoride salts”, *Journal of Nuclear Materials* 411 [2011] 51–59.
- [16] L. C. Olson, R. E. Fuentes, M. J. Martinez-Rodriguez, J. W. Ambrosek, K. Sridharan, M. H. Anderson, et al., “Impact of Corrosion Test Container Material in Molten Fluorides”, *Journal of Solar Energy Engineering* 137 [2015] 061007 (1-8).
- [17] F. Y. Ouyang, C. H. Chang, B. C. You, T-K Yeh, J-J. Kai, “Effect of moisture on corrosion of Ni-based alloys in molten alkali fluoride FLiNaK salt environments”, *Journal of Nuclear Materials* 437 [2013] 201–207.
- [18] L. C. Olson, J. W. Ambrosek, K. Sridharan, M. H. Anderson, T. R. Alle”, *Journal of Fluorine Chemistry*, 130(1)[2009] 67-73.
- [19] S. Guo, J. Zhang, W. Wu, W. Zhou, “Corrosion in the molten fluoride and chloride salts and materials development for nuclear applications”, *Progress in Materials Science*, 97 [2018] 448-487.
- [20] K. Sridharan, T. R. Allen, “Corrosion in Molten Salts”, *Molten Salts Chemistry: From Lab to Applications* [2013] 241-267.
- [21] J. Zhang, C. W. Forsberg, M. F. Simpson, S. Guo, S. T. Lam, R. O. Scarlat, F. Carotti, K. J. Chan, P. M. Singh, W. Doniger, K. Sridharan, J. R. Keiser, “Redox potential control in molten salt systems for corrosion mitigation”, *Corrosion Science*, doi.org/10.1016/j.corsci.2018.08.035
- [22] L. Olson, K. Sridharan, M. Anderson & T. Allen, “Intergranular corrosion of high temperature alloys in molten fluoride salts”, *Materials at High Temperatures* 27(2) [2010] 145-149.
- [23] A. Lervik, S. Wenner, O. Lunder, C. D. Marioara, R. Holmestad, “Grain boundary structures and their correlation with intergranular corrosion in an extruded Al-Mg-Si-Cu alloy”, *Materials Characterization* 170 [2020] 110695.

Model Transfer Cask for Automated Handling of Canisters in Storage Vaults

Kiran T. Badgujar, Arkel Ramesh, Anjali Iyer, Kunjman Singh, K. V. Ravi
Nuclear Recycle Board, Bhabha Atomic Research Centre, Mumbai- 400085

Corresponding author & Email : Kiran T. Badgujar, kirantb@barc.gov.in

ABSTRACT

India has adopted a “Closed Fuel Cycle” philosophy, where spent nuclear fuel is regarded as a material of resource. The nuclear waste management practices adopted in India are at par with international practices in accordance with the guidelines of the International Atomic Energy Agency (IAEA). The waste management practices require interim storage of Cat-III & Cat-IV high beta-gamma (alpha and non-alpha) waste canisters inside engineered storage vaults. These canisters are ultimately disposed either in deep geological repository or shielded concrete trenches depending upon their radioactivity. There is a need for development of an Automated Transfer Cask System (ATCS), which can remotely and safely transfer canisters into the interim storage vaults. The major challenge in the development of a transfer cask is remote alignment of cask with the vault-port and the subsequent remote handling of vault-lid and transfer of canister into the storage vault without breaching the shielded integrity during transfer. Thus, a scaled down model has been designed, manufactured and demonstrated successfully for automated handling of lid and transfer of canisters. The developed transfer cask comprises of motorised drives, grapplers, load cells and is equipped with PLC based control system for safe transfer of canisters. This paper describes the design philosophy, constructional features, remote handling features, safety interlocks and performance feedback gained during demonstration of the system.

Keywords: Canister, Transfer Cask, Radioactive, Storage vault, Grapppler, Repository

Introduction

Automated Transfer Cask System (ATCS) is a special type of lead shielded cask, which is planned to be used in conjunction with an EOT crane to enable automated transfer of canisters at desired storage locations of interim storage vaults. Fig. 1 shows the fully developed Automated Transfer Cask System (ATCS).

In the existing Solid Waste Storage and Surveillance Facility (SSSF), Tarapur, transfer of Vitrified Waste Product (VWP) canisters is being carried out sequentially with human intervention in batch mode [1].

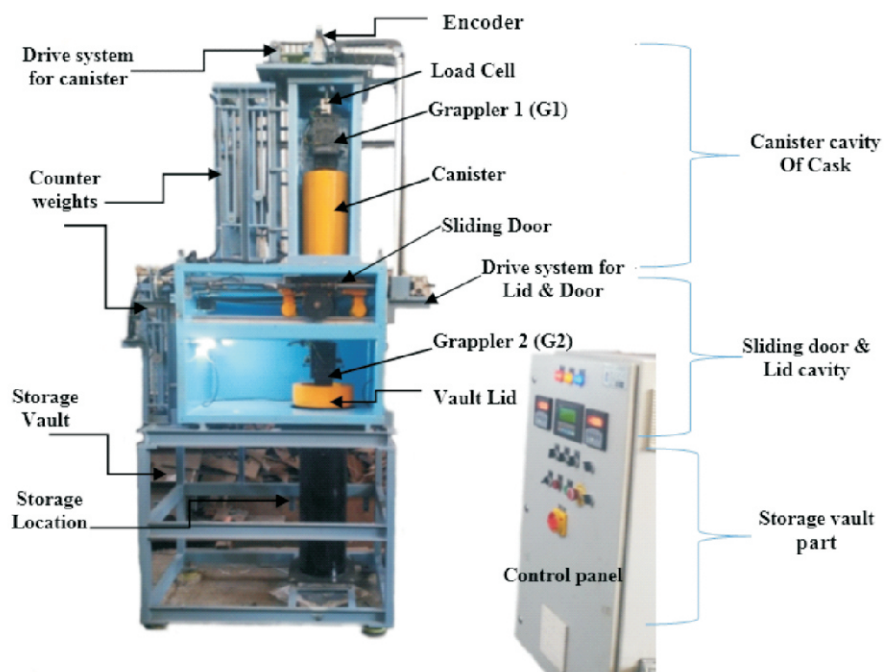


Fig. 1: The Automated Transfer Cask System (ATCS)



Fig. 2: Solid Storage and Surveillance Facility at Tarapur

Fig. 2 shows photograph of SSSF, Tarapur. At SSSF, for transfer of VWP canisters in storage vault, a shielded loading platform is placed over the vault-port and loading platform door is opened. Now, the crane hook is engaged with the vault-lid and the lid is lifted to a height within complementary shield such that loading platform door is closed without radiation streaming. Thereafter the transfer cask is kept on the loading platform where both the loading platform-door and cask-doors are opened one after the other. The canister is then transferred inside the storage vault using lifting links attached to a crane hook. The cask and loading platform doors are closed and transfer cask is taken away. Lastly, the storage location is closed by first bringing the lid held by crane within complementary shield of loading platform door. Then the loading platform door is opened and finally, the lid is placed inside the vault cavity. Similarly, unloading operations are carried out by reversing the operation sequence. The present practice has its limitations such as the process is carried out in batch mode; the process requires administrative control during handling of the vault lid & canister and the facility requires crane with higher height of lift.

In Belgium, transfer of VWP canisters is carried out using two separate transfer casks, one meant for the lid and other for canister [2]. Fig. 3 shows operational sequence for transfer of canister in storage vault. This system involves multiple number of handling equipment and series of steps for transfer of canister into storage vault.

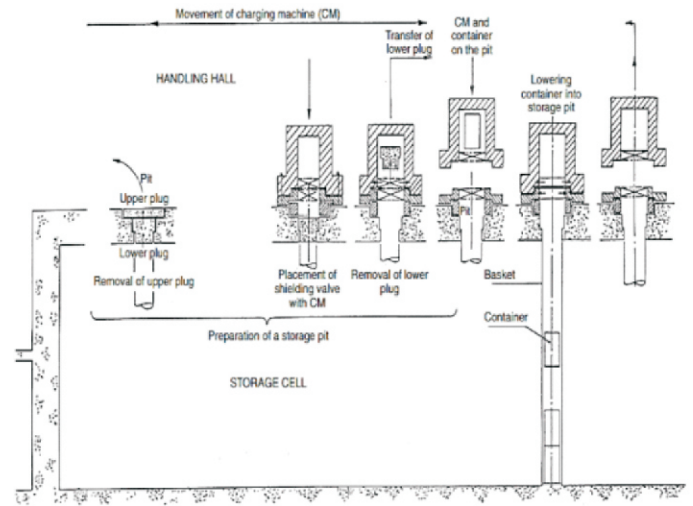


Fig. 3: Operational sequence for transfer of canister in storage vault at Belgium

Considering the rate at which the nuclear industry is growing, automation of crane & transfer cask of interim storage facilities was felt necessary. Hence, it becomes imperative to develop a transfer cask system, which automates the transfer process, reduces the number of sequential steps and limits the man-rem expenditure. In this regard, a novel scaled down model of ATCS has been designed, developed and demonstrated for automated handling of storage vault-lid (housed within the cask shield cavity) & transfer of canister from cask to vault and vice versa.

System Description

The developed system is a scale down model of ATCS. The system is divided into three zones; first zone has a canister cavity containing grapples G1 for handling of canister along with its motorized drive system. The second middle zone has a sliding shielded door and lid cavity containing grapples G2 for handling of vault-lid and motorized drive mechanism for up & down movement of grapples as well as for movement of sliding door. The third zone depicts the dummy storage vault for simulating the vault lid storage as well as canister storage.

The system is provided with end limit switches, encoders and load cells for its automated operation using PLC. The system is designed for operation in Auto & manual mode using interlocks and in admin mode during maintenance. Operational sequence of loading cycle is described below.

- Placement of ATCS on storage location i.e. vault port.
- Lowering the lid grapppler G2 and engage with vault-lid.
- Lifting the lid using G2 up to the Top Dead Centre (TDC).
- Opening the sliding door along with vault- lid in the door & lid cavity.
- Lowering the canister into storage vault till its bottom most position and disengage the canister grapppler G1.
- Retracting G1 back to the home position.
- Closing the sliding door along with vault- lid attached to G2.
- Lowering the G2 and placement of vault-lid into the vault.
- Taking the G2 to home position and lift the ATCS for next consignment.

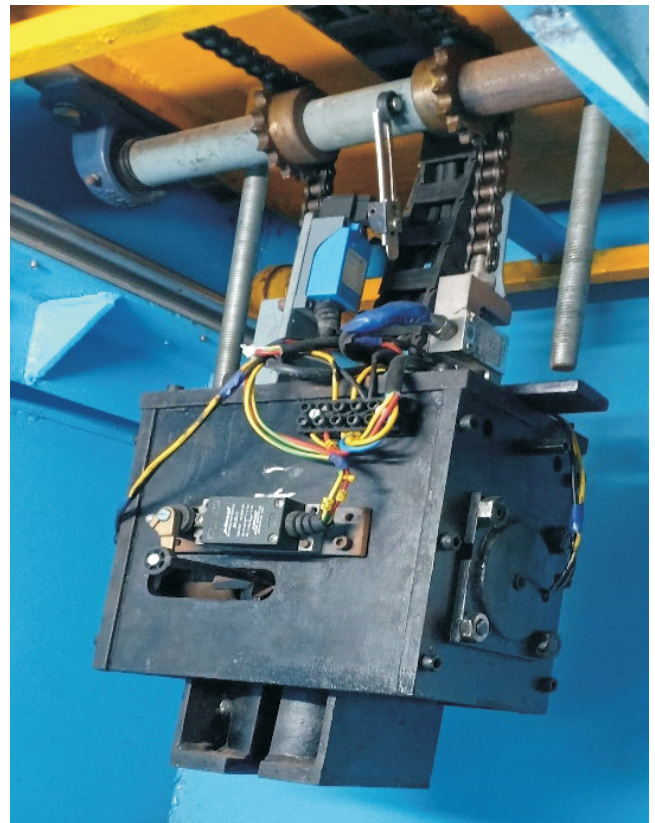


Fig. 4: Electro-magnetic Grapppler

Similar operations shall be carried out for unloading cycle by reversing the operation ‘e’. It can be observed from above sequences that in the whole process, the lid is confined within the ATCS shielding cavity itself thereby maintaining the integrity of the storage vault at all times and the confined space is relentlessly maintained which eliminates the chances of radiation streaming.

Main System Components & Special Features

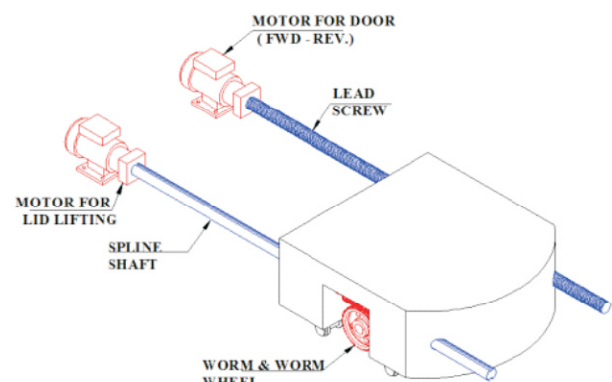
Following are the main components of ATCS: (i) Grapppler (ii) Vault lid (iii) Load Cell (iv) Sliding Door (v) Drive system and (vi) Control Panel.

(i) Grapppler: Fig. 4 shows Normally closed type (fail/safe) Electromagnetic grapppler developed for handling of vault lid and canister. Electromagnets are actuated only when grapppler fingers are needed to be opened for handling of canister/lid. In case of failure of electrical supply, the grapppler retains grip position by spring force. In addition, manual override provision is provided in the grapppler to disengage the jaws from outside the cask using remote tool.

(ii) Vault lid : Vault lid is a part of storage vault and provides radiation shielding to vault port. The thimble of vault lid is made compatible for remote handling with grapppler jaws.



(a)



(b)

Fig. 5: Sliding Door (a) & its associated mechanism (b)

(iii) Load Cell : In addition to limit switches, load cell is required to detect presence, absence or stuck-up of canister or lid during transfer. The system has been provided with two load cells placed between grapppler and lifting chain.

(iv) Sliding Door : The sliding door provides shielding and also facilitates handling of lid. A special type of drive mechanism as shown in Fig.5 was needed for integrated movement of door as well as handling of vault lid. In order to achieve this, sliding door has been provided with two drives, i.e. lead screw drive for movement of door and secondly, spline shaft fitted with worm drive for handling of vault lid. The handling of vault lid is achieved by rotation of splined shaft which rotates worm wheel even when the sliding door is stationary and as worm wheel is attached to lifting chain sprocket for vertical movement of the grapppler G2. The spline shaft also facilitates movement of vault lid within the cask cavity when sliding door opens and closes during the transfer operation without any entanglement of electrical cables.

(v) Drive System : The drive system comprises of three sets of induction motors and gear boxes corresponding to the three different motions required. First motion involves the chain and sprocket drive to lift and lower the canister via grapppler G1, second motion also involves chain and sprocket drive coupled with worm wheel drive to lift and lower the lid via grapppler G2 and the third motion consists of lead screw drive for movement of sliding door for its opening and closing. All the three drives have been provided with manual override features to operate the drives independently during emergency.

(vi) Control Panel : The control panel is PLC based and equipped with an HMI to visualize and operate the system in auto, manual or admin mode. Fig.6 shows the photograph of control panel. Any alarms, indications or faults are noticeable in the HMI. Emergency button is provided to terminate all the operation instantaneously. The control panel has Toggle type switches, Push Buttons, Selector Switches for manual operation of the system. The panel also has digital display for load cell readings. The PLC logic has two different programs for storage (Disposal) and retracting (retrieving) cycles which operator has to select before commencement of



Fig. 6: Control panel



Fig. 7: Lever type limit switch



Fig. 8: Load Cell



Fig. 9: Tooth type proximity sensor



Fig. 10: Encoder

auto or manual mode operations. Automated and safety interlock operation of system is achieved by sensing the feedback of lever type limit switches, encoder, tooth type inductive proximity sensors and load cells.

Fig. 7, 8, 9 & 10 depict various sensors used in the system. Cable take-up and management of lifting chain during its up&down movements were resolved using drag chain and counter weight arrangements respectively.

System Safety Interlocks

Following safety interlocks are incorporated for Auto & Manual mode operations.

- a) The Reverse / Forward motion of Cask Shielded Sliding door is enabled only if Canister Grapppler G1 is at its stop most position and Vault Lid lifting Grapppler G2 is loaded & is at its top most position.
- b) During Canister Disposal cycle, Canister DOWN motion is enabled only if load cell measures the weight of canister and shielding door is in fully opened position.
- c) During Canister retrieval cycle, Grapppler G1 DOWN motion is enabled only if load cell measures No weight and shielding door is in fully opened position.
- d) Vault Lid lifting Grapppler G2 up/down motion enable only if sliding door is fully closed.
- e) Both Grapplers open (un-grip) only when respective load cells measure No Load.
- f) Lid Grapppler (G2) interlocks for jaws opening (un-grip) and closing (grip) are different for lid lifting and lid unloading operation.
 - Lid loading/lifting operation: Lid Grapppler (G2) Jaws open 50 mm prior to lid lifting thimble position measured by encoder and closes at lid lifting position and lid lifted till it reaches its top most position.
 - Lid unloading/lowering operation: Lid Grapppler (G2) Jaws open only when lid reaches its bottom most storage location sensed by limit switch & load cell and closes immediately after 50mm up motion of grapppler measured by encoder.
- g) Canister Grapppler (G1) interlocks for Jaws opening and closing are different for canister disposal and retrieval cycle.
 - Disposal cycle: Canister Grapppler (G1) Jaws open only when canister reaches its bottom most storage location sensed by limit switch & load cell and closes immediately after 100mm up motion of grapppler measured by encoder.
 - Retrieval cycle: Canister Grapppler (G1) Jaws open 100 mm prior to canister lifting position measured by encoder and closes at canister

lifting position and canister lifted till it reaches its top most position.

- h) Load cell interlocks for Canister and Vault lid vertical up/down movement are different for loading & unload cycle:

Experience Gained During Performance Trials

Due to developmental nature of the system, the system has been tested repeatedly to generate base line data and ensuring safety during the operation. Following are major improvisation incorporated in the system design.

- a. **Underweight/Overweight alarm:** During lowering operation, in an event of the canister or lid getting stuck in its path, the load cell shall detect the underweight and PLC will raise Underweight alarm and terminates the operation. Furthermore, during lifting operation, if canister/lid stuck-up in its path, load cell will detect the overweight and PLC will raise overweight alarm and terminates the operation.
- b. **Incorporation of Load cells:** Safety interlocks are different for loading and unloading cycles. Hence, in addition to limit switches & encoders, load cells were introduced in both canister & lid grapplers to identify presence of canister/lid. Hence, load cell plays vital role in automation & safety of this system.
- c. **Grapppler Electromagnetic Coil Over-heating:** To avoid overheating of electro-magnetic coil of grapppler, the time of actuation is kept as low as possible and this has been achieved using encoders feedback

Future Scope

The developed ATCS demonstrates retrieval and disposal for single canister. However, interim storage vault houses minimum 3 canisters stacked one above the other. Future scope in design of ATCS shall involve modification of PLC program for transfer of 3 canisters. In the auto cycle, PLC shall first execute dummy cycle to ascertain the presence and actual position of canisters inside vault.

Instead of lifting/lowering of ATCS using crane during alignment with port, ATCS will remain 100 mm above surface floor of vault and local shielding shall be moved

up & down for maintaining radiation integrity. This shall simplify the crane design.

Conclusion

The model Automated Transfer Cask System has been tested and demonstrated successfully. The system not only serves in reducing the man-rem expenditure of the material handling personnel but also simplifies the remote emplacement of canister in the storage vault with adequate safety and reliability. The experience gained in the demonstration trials of ATCS will pave the way for execution of plant scale “Automated Transfer Cask System” meant for active plant operations.

Acknowledgments

The authors are thankful to Shri Vismai Singh, SO/D, NRB and Shri B. S. Jatav, TO/D, NRB for their contribution in design & inspection of Instrumentation & electrical system respectively. Authors are also thankful to Shri R. Srinath, SO/D, NRB for his support in preparation of this report.

References

- [1] S.D. Misra, Developments in Back End of the Fuel Cycle of Indian Thermal Reactors, Energy Procedia 7 (2011), page no. 474-486.
- [2] Interim Storage of Radioactive Waste Packages, TECHNICAL REPORTS SERIES No. 390, IAEA, Vienna, 1998, page no. 55-58.

Development of In-situ X-ray imaging and μ -CT facility under load conditions at imaging beamline Indus-2

Ashish K. Agarwal¹, Payal Singhai¹, B. Singh^{1, 2},
Yogesh Kashyap^{1, 2} and Mayank Shukla^{1, 2}

¹Technical Physics Division, Bhabha Atomic Research Centre, Mumbai-400085

²Homi Bhabha National Institute, Anushaktinagar, Mumbai-400094

Corresponding author & Email : Ashish K Agarwal, ashishka@rrcat.gov.in

ABSTRACT

Synchrotron based X-ray micro tomography is a versatile technique to study material microstructure, density, composition etc. Especially under variable load conditions, such studies are extremely important to evaluate material behavior in real life applications. We have developed an in-situ X-ray micro tomography facility at imaging beamline Indus-2 to study material microstructure under compression and tensile load conditions. This allows visualization as well as image based quantitative analysis of microstructural changes under external loads and obtains its correlation with mechanical, and transport properties. In this report, we have discussed the details of this experimental facility, challenges, advantages and a case study of Aluminium (Al) foam sample under compression load.

Keywords: In-situ loading, X-ray tomography, synchrotron imaging, material microstructure

Introduction

Microstructure, along with physical properties of constituent material phases, plays an important role in defining the macroscopic properties of the material. Deformation mechanism, strain accumulation and localization, cracks initiation and failure under load during operation, are extremely important properties of materials for deciding their utility in real-life applications^{1,2}. A strong and defining correlation of microstructure with mechanical and transport properties of materials is established through empirical numerical relations or finite element modeling³⁻⁵. Advanced materials such as polymers, ceramics, composites, bio-materials etc. are being designed and developed with specific microstructure, density and composition to achieve desired mechanical and transport properties⁶⁻⁸. 3D evaluation of microstructure is conventionally done using electron microscopy with successive serial sectioning of the sample but modification of structure during sample preparation leads to some ambiguity in the structure property relation models^{9,10}. In-situ micro-tomography, which provides 3D microstructure and density map with high resolution and contrast at different load conditions is one of the most suitable techniques for this purpose¹¹.

Among various mechanical loads, compression and tensile stress is most commonly encountered in practical conditions¹²⁻¹⁴. Therefore we have developed a facility for carrying out synchrotron based high resolution and high contrast X-ray micro-CT experiments under in-situ compression or tensile load conditions. In this report, we discuss details of the experimental facility developed at Imaging beamline, Indus-2 synchrotron source, RRCAT Indore, and a case study of Aluminium (Al) foam under compression load.

Materials and Methods

For In-situ X-ray micro-CT experiment under compression mode, samples of standard size need to be prepared either in cubic/cuboidal or cylindrical form. The height of the sample need to be 15 mm, which can be compressed upto 5 mm. In tensile mode, sample need to be prepared in the form of dog-bone shape for which active length between jaws should be 10 mm before initiating the tensile loading which is stretched upto maximum 20 mm. In-situ experiments require acquisition of several micro-CT scans at different loading condition under the identical beam and detector conditions. A faster rate of data acquisition (typically few minutes per scan) at Synchrotron beam is particularly important to acquire

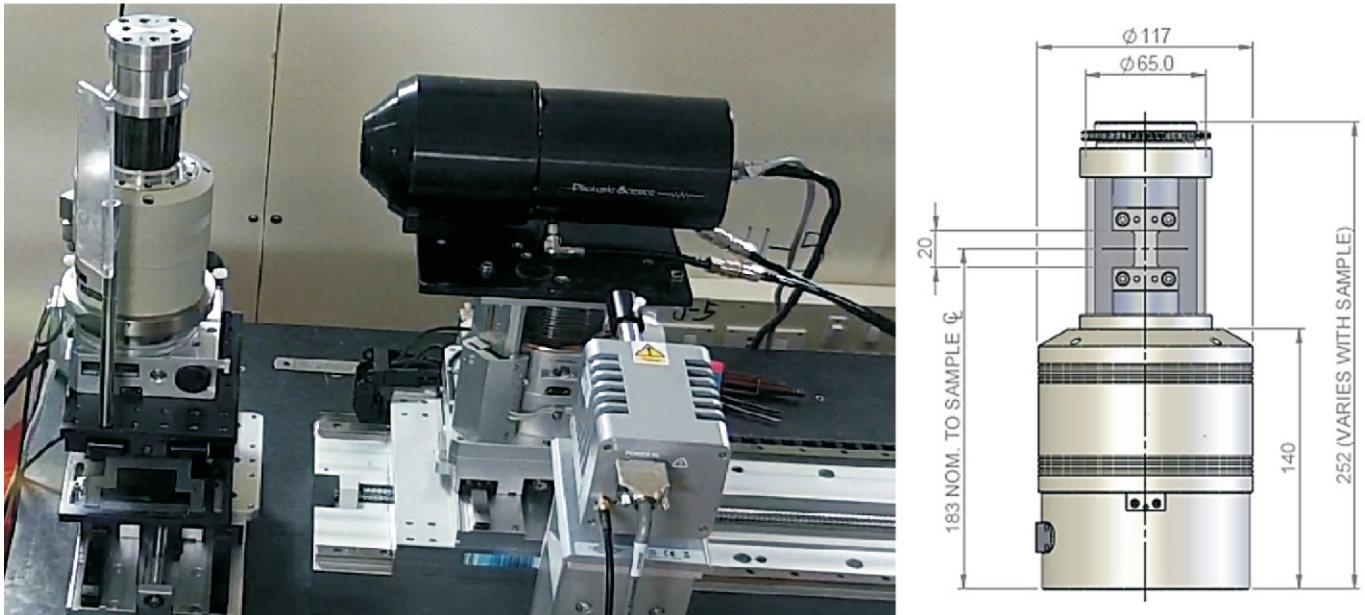


Fig. 1: The In-situ X-ray μ CT facility at imaging beamline, BL-4 of Indus-2 and design of In-situ compression and tensile stage

several such scans at different loading conditions, which in turn, is helpful in analysis of stress-strain behavior of materials, and defining structure-property relation. The facility for In-situ X-ray micro-CT developed at imaging beamline consists of synchrotron beamline operated in monochromatic and white beam modes, a sample rotation stage, a high resolution, high frame rate X-ray imaging camera, manipulation system for sample and detector to allow their alignment by orthogonal translation and rotation, and an In-situ loading device (Fig. 1)¹⁵. The system is equipped with 500 N & 3000 N load cell with 1% accuracy. The smallest step of load applied is 1/1000 fraction of maximum range of load cell being used. The samples can be compressed or pulled with speeds in the range 0.1 mm/minute to 1 mm/minute.

Data acquisition protocol and automation

Data acquisition for In-situ micro-CT experiments includes several tasks such as optimization of experimental parameters, sample alignment with beam and camera, applying suitable load or extension to the sample, collection of micro-CT scan data at different load condition, re-initialization of set-up after each micro-CT scan and collection of reference, background images. The first tomography scan of the sample is taken initially in the unloaded condition and then sample is stepwise loaded to a predefined stress (loads) or strains (extensions). At each loaded position, micro-CT scan is taken while keeping the sample at constant load/extension. Entire process is carried out remotely from the control room by establishing remote communication of in-situ rig controller from control room

PC without any human intervention once it is initiated by user.

Post processing and analysis

Each micro-CT scan data is normalized, background corrected and then tomography reconstruction is carried out. The quantitative parameters from micro-CT projections and reconstructed slice images under various load conditions are derived. Variation of measured parameters such as porosity, pore size, shape, etc. can be studied with load. These microstructural properties are related to stress-strain behavior and other physical properties of materials through empirical relations or finite element modeling. The study is also useful for visualization of strain field mapping, strain localization at pores, voids, interfaces, cracks and inclusions geometry, surface under load condition, and measures their capacity to cause fracture in the materials. Other potential studies are 3D fatigue crack initiation and propagation under cyclic load and its dependence on cracks, microstructure, pores, particles, surface, defects, dislocation etc.

Case Study: Al foam under compression load

We have carried out In-situ X-ray micro-CT study under compression mode on several materials such as polyurethane foam, metal foam (Al) and Polymer fiber aerogels materials. As an example study, aluminum foam sample under compression is presented here. An Al foam sample of dimension 6.4 mm x 6.2 mm x 14.4 mm was first extracted from the large block of sample. The initial load measured at this position was offset to zero and In-situ

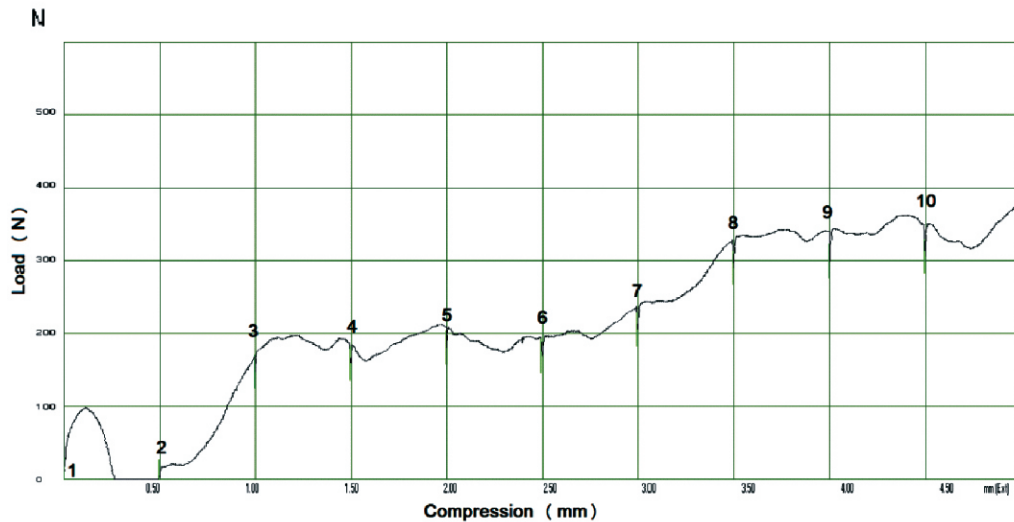


Fig. 2: Load vs. compression curve for In-situ compression of Al foam sample

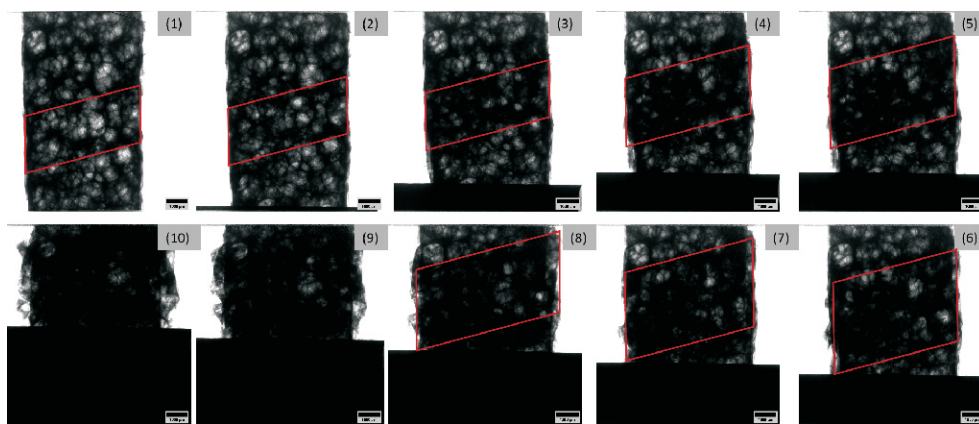


Fig. 3: X-ray projection images of Al foam at different compression loads. Sample densification with load and buckling is highlighted in red quadrangle

micro-CT scan was completed under this unloaded conditions. Further to this, automated data acquisition code was run to carryout complete in-situ loading micro-CT scan in total 10 steps with extensometer increments of 0.5 mm at each step until the sample was crushed at approximately 400 N loads. The force compression curve shows (Fig. 2) an initial rise and then fall in the force during first compression of 0.5 mm. In the second compression step of 0.5 mm, elastic behavior with linear rise in load with compression is observed. From 3rd to 6th compression, no further rise in the force is seen with increasing compression which is first densification region. Again, at 7th compression, some rise in the force is seen followed by further densification of the sample in 8th to 10th compression. This behavior of force-compression curve need to be explained by microstructural changes in the samples.

Fig. 3 shows the first projection images of the sample at different compression conditions. These images clearly show that there is a region in the sample (highlighted in the

red quadrangle), which is more specifically compressed under load. As the load increases, the densification of that particular region also increases whereas other regions of the samples are more or less unaffected until the compression reaches to 6th position. This particular phenomenon in mechanical engineering is known as strain localization and strain band formation in the sample¹⁶. All the compression applied to the sample is localized and transferred to the strain bend until a specific level of compression. Further compression leads to the densification of other regions too which is reflected in the projection images of 6th to 10th steps of compression. Observation of these projection images under compression load partially explains the behavior of Al foam sample in force-compression curve.

In order to get more insight to the microstructural changes in Aluminum foam under load, the vertical micro-CT slices of the sample under different load conditions are shown in Fig. 4. The reconstructed slice images clearly show the cellular microstructure of the foam which is

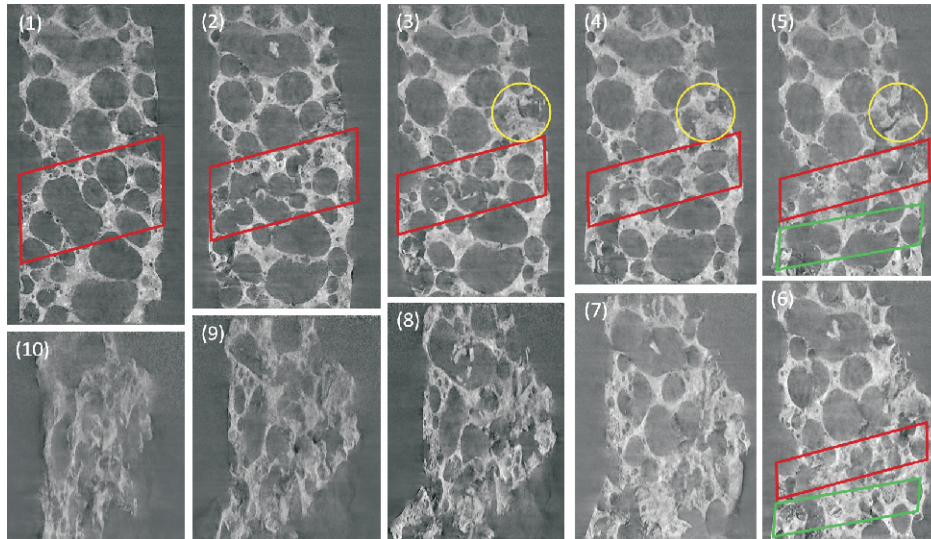


Fig. 4: Tomographic slice images at identical depth in the sample show microstructural changes in the Al foam. Cell collapse band in the middle is highlighted in red quadrangle

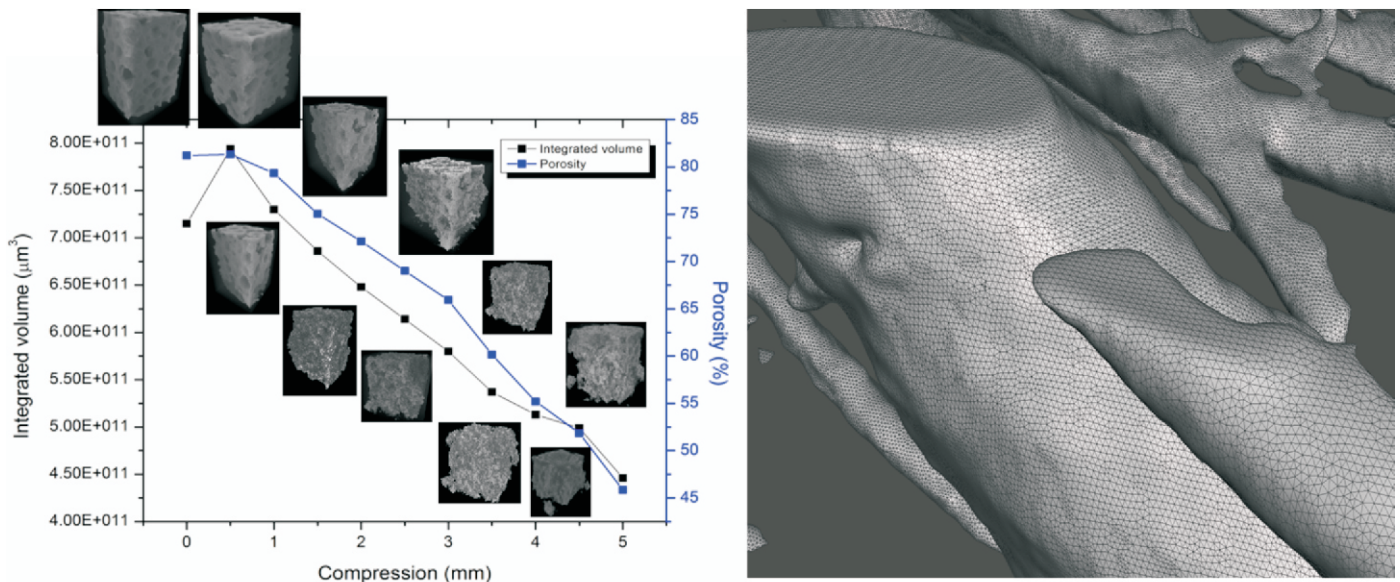


Fig. 5: Quantitative variation of porosity, integrated volume and 3D volume images of sample with compression. 3D volume mesh data generated from the micro-CT data

composed of interconnected large open cells of various sizes separated by Aluminum struts of varying thicknesses. The struts also enclose some closed pores of small volumes at random locations. When load is applied, it affects the shape, size of cellular structure and struts. It is seen in the foam of cell volume reduction, cell wall breaking etc. leading to densification of the sample as observed in the projection images in Fig. 3. The initial dip observed in the load compression curve is due to sudden breaking of certain struts and collapse of some cells in the region highlighted in the red quadrangle in Fig. 4. This collapse of the cells is due to brittle nature of aluminum and strain localization at the thin walled struts in that region. Further load leads to reduction in the cell volume in the form of elastic deformation at the 2nd compression step followed by plastic deformation which is seen in form of

densification observed in load compression curve and projection images from steps 3rd to 6th compression. Further compression leads to elastic deformation and cell collapse in the second quadrangle region highlighted in the green, which is seen at 7th to 10th compression.

Discussion

The microstructural changes in the cellular structure and struts of Aluminum foam sample under in-situ compression load are observed in the form of cell volume reduction, cell collapse, and strut breaking etc. which clearly explain its compression behavior. Quantification of porosity and integrated volume of the sample at different load conditions and their corresponding 3D images are shown in Fig. 5. This plot identifies that both, the volume as well as porosity of the sample reduces as the load

increases which is seen in the force-compression curve of the sample. Further to this, 3D mesh data of Al foam sample in unloaded condition is also generated as shown in Fig. 5, which can further be used for finite element modeling of the sample to establish structure-property relations.

Conclusion

In-situ micro-CT facility developed at imaging beamline is useful in studying microstructural variation in the materials under compression and tensile load condition and establishing correlation of these changes with its deformation behavior. A case study of Al foam sample under compression load is presented to show the potential of the facility. In this experiment, the compression behavior of Al foam is quite clearly explained through underlying microstructural changes in the cellular shape, size, volume, porosity and strut breaking. Strain localization, stain band formation and sample buckling are some of the effect causing the peculiar force compression curve of the sample recorded during in-situ micro-CT experiment. Further development of this In-situ X-ray micro-CT facility is planned under other mechanical loads such as impact, shear and torsion loading as well as under thermal load condition at elevated and cooled temperatures.

Acknowledgments

Authors acknowledge Dr. S.M. Yusuf, Associate Director Physics Group and Dr. T.V.C. Rao, Head Technical Physics Division for their support and encouragement in beamline development and utilization activity of imaging beamline. Authors also acknowledge the support provided by Dr. S. Saxena AMPRI Bhopal for proving test sample used in the image based testing of the set-up. We are also thankful to RRCAT Indore, particularly Indus synchrotron operation division for providing the beam time for the experiments.

References

- [1] E. Maire, A. Fazekas, L. Salvo, R. Dendievel, S. Youssef, P. Cloetens, and J.M. Letang, *Compos. Sci. Technol.* 63, 2431 (2003).
- [2] B.M. Patterson, N.L. Cordes, K. Henderson, X. Xiao, and N. Chawla, *Microsc. Microanal.* 24, 1002 (2018).
- [3] P. Kenesei, A. Borbély, and H. Biermann, *Mater. Sci. Eng. A* 387–389, 852 (2004).
- [4] J. Réthoré, N. Limodin, J.Y. Buffière, F. Hild, W. Ludwig, and S. Roux, *J. Strain Anal. Eng. Des.* 46, 683 (2011).
- [5] B. Rousseau, J.Y. Rolland, P. Echegut, E. Brun, and J. Vicente, *J. Phys. Conf. Ser.* 369, (2012).
- [6] J.G.F. Wismans, L.E. Govaert, and J.A.W. Van Dommelen, *J. Polym. Sci. Part B Polym. Phys.* 48, 1526 (2010).
- [7] T. Fey, B. Zierath, P. Greil, and M. Potoczek, *J. Porous Mater.* 22, 1305 (2015).
- [8] J. Banhart, F. García-Moreno, K. Heim, and H.-W. Seeliger, 61 (2019).
- [9] S. Englisch, J. Wirth, T. Przybilla, B. Apeleo Zubiri, J. Wang, N. Vogel, and E. Spiecker, *Microsc. Microanal.* 25, 392 (2019).
- [10] Y. Zhao, W. Zhang, B. Koe, W. Du, M. Wang, W. Wang, E. Boller, A. Rack, Z. Sun, D. Shu, B. Sun, and J. Mi, *Mater. Charact.* 164, (2020).
- [11] E. Maire, S. Grabon, J. Adrien, P. Lorenzino, Y. Asanuma, O. Takakuwa, and H. Matsunaga, *Materials (Basel)*. 12, 1 (2019).
- [12] E. Linul, C. Vălean, and P.A. Linul, *Polymers (Basel)*. 10, (2018).
- [13] D. Zeleniakiene, P. Griškevičius, and V. Leišis, *Mechanika* 3, 22 (2005).
- [14] T. Dillard, F. N'Guyen, E. Maire, L. Salvo, S. Forest, Y. Bienvenu, J.D. Bartout, M. Croset, R. Dendievel, and P. Cloetens, *Philos. Mag.* 85, 2147 (2005).
- [15] A.K. Agrawal, B. Singh, Y.S. Kashyap, M. Shukla, P.S. Sarkar, and A. Sinha, *J. Synchrotron Radiat.* 22, 1531 (2015).
- [16] H.W. Chai, Z.L. Xie, X.H. Xiao, H.L. Xie, J.Y. Huang, and S.N. Luo, *Int. J. Plast.* 131, (2020).

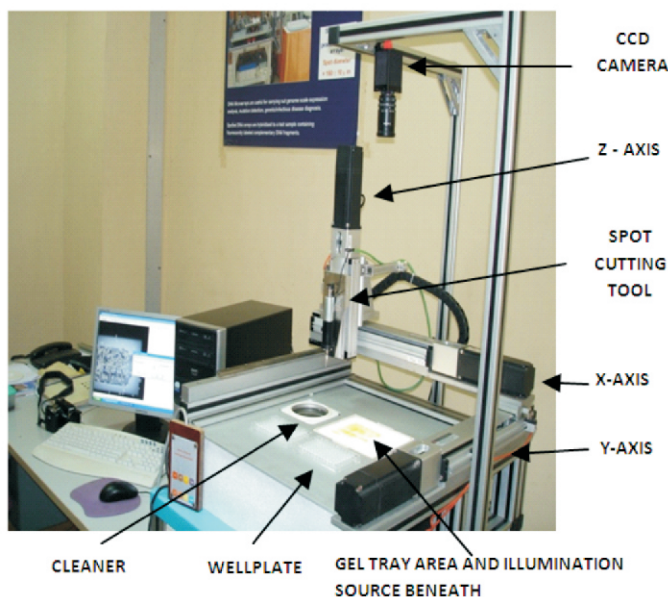
Spot Picker Robot for Proteomics Applications

In discovering new proteins for developing biomarkers for new diagnostic tests

Proteomics is a well established subject in medical science, which focuses on the library of proteins specific to a given bio-system, the proteome, and understanding of relationships therein. Analysis of 2D gel electrophoresis (2DGE), by imaging and unequivocally identifying the various protein spots is the most important and challenging step in proteomics. The spot picker robot can be seen as an essential tool in proteomics. It accurately locates and identifies the protein spots from 2D gels and picks and transfers the proteins for further analysis, thus enhancing data quality and reliability in the field of proteomics. The application of this robot has helped in discovering new proteins to develop biomarkers for new diagnostic tests. It provides the necessary automation for high throughput analysis. The spot picker robot features non-separable wavelet based novel imaging algorithms, enhanced illumination for detection of faint, irregular and overexposed protein spots in a nonlinear background and a high performance solenoid controlled surgical grade protein spot excision tool.

This robotic system is being developed as low cost substitutes for higher cost imported system and it

demonstrates state-of-the-art technology in precise positioning and powerful imaging algorithm in the field of proteomics. The system is installed at RMC, Parel and is under clinical use. The technology has been transferred to a private firm for commercialization in February 2021.



Spot Picker Robot



Protein Spot Cutting Tool



2DGE Image Analysis

By Dr. R. S. Sengar, DRHR, BARC

Climate change impact on glacier melting in Himalayas

Understanding glacier variability and local moisture recycling are crucial to understanding the potential risks to Himalayan ecology. Isotope studies could provide interesting clues

By Tirumalesh Keesari

Glaciers, being an integral part of the Earth's natural system, serve as the most reliable and sensitive indicators of climate change. Besides, they constitute a significant component of the hydrological regime. It is estimated that over 10,000 glaciers are receding at a rate of 100 to 200 feet (30 to 60 metres) per decade in the Indian Himalayas. In fact the melting is twice as fast since the year 2000 as they were 25 years before, due to human induced climate change. And it is projected that two-thirds of Himalayan glaciers will vanish by the end of this century if the current rate of greenhouse gas emissions continue (Ann Rowan, 2020).

Another threat from warming temperatures is that of formation and bursting of glacial lakes. With warming, the temperature around ice cover stays at $-2\text{ }^{\circ}\text{C}$ compared to much cooler temperatures earlier (-20 to $-6\text{ }^{\circ}\text{C}$), (Dailysabah, 2021). Though the ice is still frozen, it is closer to its melting point and so it takes less heat to trigger an avalanche than some decades ago. This avalanche is termed as Glacial Lake Outburst Flooding (GLOF), and many such avalanches were reported in the past. In fact, some suspect GLOF as the cause of recent disaster on 7th February 2021 in Chamoli district (Uttarakhand, India), most notably in the River Dhauliganga. Whether this particular disaster was caused by climate change or not, may be point of debate. But it is certain that the climate

Tracers like Deuterium, Tritium, Oxygen-18 of water molecule and other dissolved isotopes have potential applications in climate studies including glacier dynamics, for isotopes being part and parcel of water molecules can trace the movement of large water masses more accurately

change can trigger natural disasters or increase the landslides and avalanches because the valleys that were earlier packed with ice open up due to warming, and this creates space for landslides to enter into, which allows the rock pieces to move downhill more easily amassing a great force.

Such disasters underscore the fragility of the Himalayan mountains where the lives of millions are being affected by climate change. It would be pertinent to assess beforehand the hazards posed by breaching of expanding lakes, considering the increased rate of occurrences and the mammoth damage they cause to human life, property as well as overall health of ecosystem.



Photo Credit @ Om Kumar, JNU, Delhi; DAE BRNS and BARC

For the first time, $\delta^{17}\text{O}$ isotope has been used in the Indian context to infer the influence of local moisture recycling at the continental site. These studies of DAE-BRNS provide new evidence that improves the current understanding of the forcing factor behind glacier advances and retreat in the Western Himalayas

Environmental isotopes along with other spatial techniques have been used to understand the impact of climate on glacier melting in parts of western Himalaya. Isotopes being part and parcel of water molecules can trace the movement of water masses more accurately than other tracers. The isotope tracers like Deuterium, Tritium, Oxygen-18 of water molecule and other dissolved isotopes have potential applications in climate studies including glacier dynamics.

Some of these research activities are funded and guided by DAE through BRNS program. Isotope Hydrology Section of Isotope and Radiation Application Division (BARC) has provided technical support in setting up of water isotope measurement facility at JNU, New Delhi and played a key role in the implementation of climate change project at Chhota Shigri Glacier, Himachal Pradesh. The outcome of these projects highlight the dominant role of Westerlies over Indian Summer Monsoon on glacier variability in the Himalaya during Late Quaternary Period (Om Kumar et al., 2021; Naveen Kumar *et al.*, 2018). Also, the studies provide new evidence that improves the current understanding of the forcing factor behind glacier advances and retreat in the Western Himalaya. For the first time, $\delta^{17}\text{O}$ isotope has been used in the Indian context to infer the influence of local moisture recycling at the continental site (Ranjan *et al.*, 2021).

References

- Ann Rowan, 2020; <https://phys.org/news/2020-08-two-thirds-glacier-ice-himalayas-lost.html>
- Daily Sabah, 2021; <https://www.dailysabah.com/life/environment/glacier-disaster-in-himalayas-spotlights-climate-change-risks>
- Om Kumar, AL. Ramanathan, Jostein Bakke, B.S. Kotlia, J.P. Shrivastava, Pankaj Kumar, Rajveer Sharma, Pramod Kumar, Role of Indian Summer

Monsoon and Westerlies on glacier variability in the Himalaya and East Africa during Late Quaternary: Review and new data, *Earth-Science Reviews* 212 (2021) 103431, <https://doi.org/10.1016/j.earscirev.2020.103431>

- Naveen Kumar, AL. Ramanathan, Tirumalesh Keesari, S. Chidambaram, ShyamRanjan, Mohd. Soheb and Martyn Tranter, “Tracer based estimation of temporal variation of water sources: an insight from supra and subglacial environment”, *Hydrological Sciences Journal*, 2018, <https://doi.org/10.1080/02626667.2018.1526381>
- Shyam Ranjan, Ramanathan AL, Tirumalesh Keesari, Virendra Singh, Naveen Kumar, Manish Pandey, Markus C. Leuenberger, “Triple water vapour–isotopologues record from Chhota Shigri, Western Himalaya, India: a unified interpretation based on $\delta^{17}\text{O}$, $\delta^{18}\text{O}$, δD and comparison to meteorological parameters”, 2021. *Front. Earth Sci.* 8 : 599632. <https://doi.10.3389/feart.2020.599632>



Dr. Tirumalesh Keesari is a Scientific Officer-G in Isotope Hydrology Section of Isotope Radiation and Application Division (BARC) and also Associate Professor in Chemical Sciences (HBNI). His research interests include water contamination, geochemical modeling, groundwater recharge, spring revival in Himalayan regions, coastal salinity and studies on extreme climatic regions of India through application of isotope

technologies. He has over 80 international journal publications to his credit and also a recipient of DAE Science and Technology Award and Indo-US Science and Technology Award.

This page is intentionally left blank

Back Page Photo: Dr. Homi Jehangir Bhabha, Dr. Homi Sethna and Dr. A.S. Rao inside a newly commissioned facility in Trombay (1956-58).
(DAE Archives)



Edited & Published by:
Scientific Information Resource Division
Bhabha Atomic Research Centre, Trombay, Mumbai 400 085, India
BARC Newsletter is also available at URL:<http://www.barc.gov.in>